

Supporting information

Thermal Driven Phase Transition of Manganese Oxide on Carbon Cloth for Enhancing Performance of Flexible All-Solid-State Zinc-Air Battery

Song Chen,^a Xinxin Shu,^a Huaisheng Wang,^b and Jintao Zhang^{a,*}

^{a.} *Key Laboratory for Colloid and Interface Chemistry, Ministry of Education, School of Chemistry and Chemical Engineering, Shandong University, Jinan 250100, China. E-mail: jtzhang@sdu.edu.cn*

^{b.} *School of Chemistry and Chemical Engineering, Liaocheng University, Liaocheng 252000, China.*

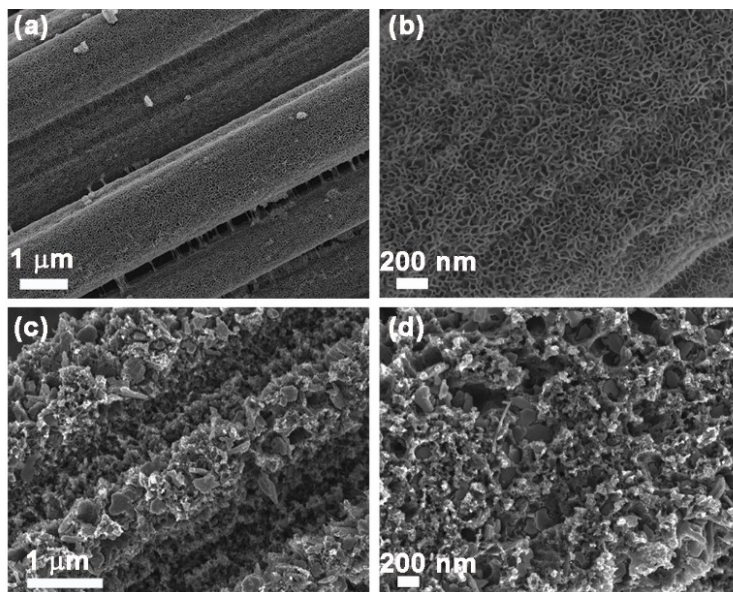


Figure S1. SEM images of MnO_x-CC-350 (a-b) and MnO_x-CC-450 (c-d) with different magnifications.

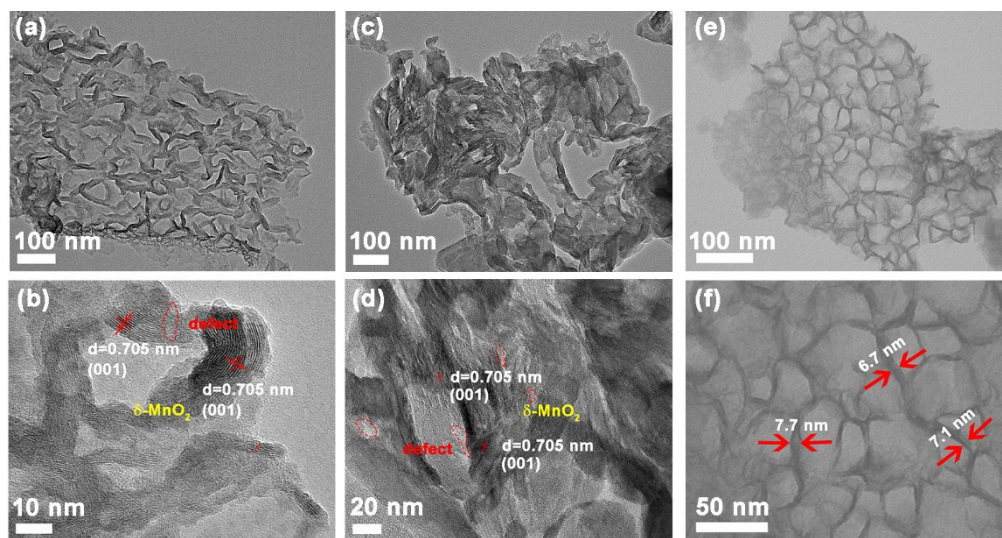


Figure S2. High-resolution TEM images of MnO_x-CC-350 (a, b), MnO_x-CC-450 (c, d) MnO_x-CC-400 (e, f).

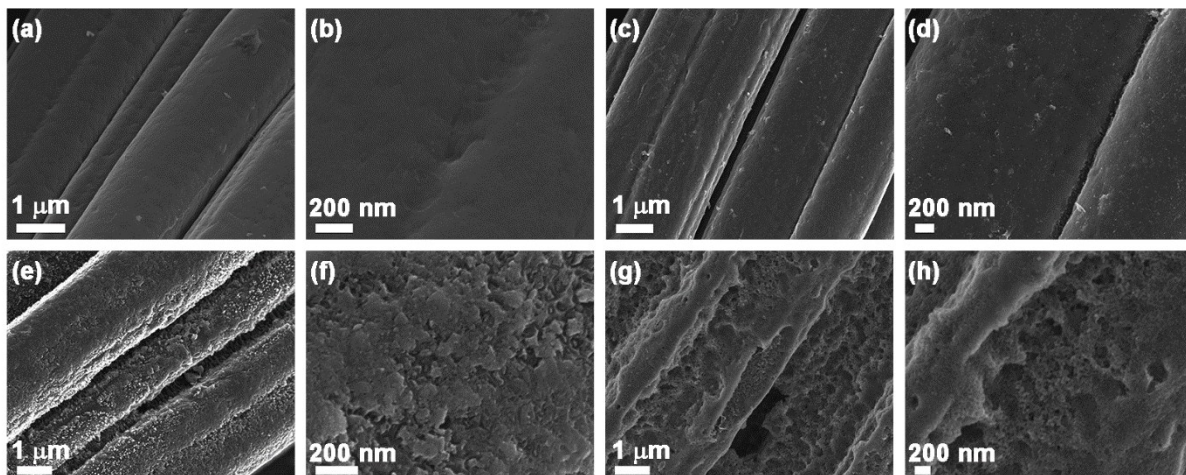


Figure S3. SEM images of MnO_x-CC (a-b), MnO_x-CC-350 (c-d), MnO_x-CC-400 (e-f), MnO_x-CC-450 (g-h) acid treatment in 3 M HCl for 24 h.

After the removal of manganese oxide by acid washing, the SEM images exhibit the highly porous surface of carbon fiber, which would be contributed the redox reactions between manganese oxide and carbon under thermal treatment.

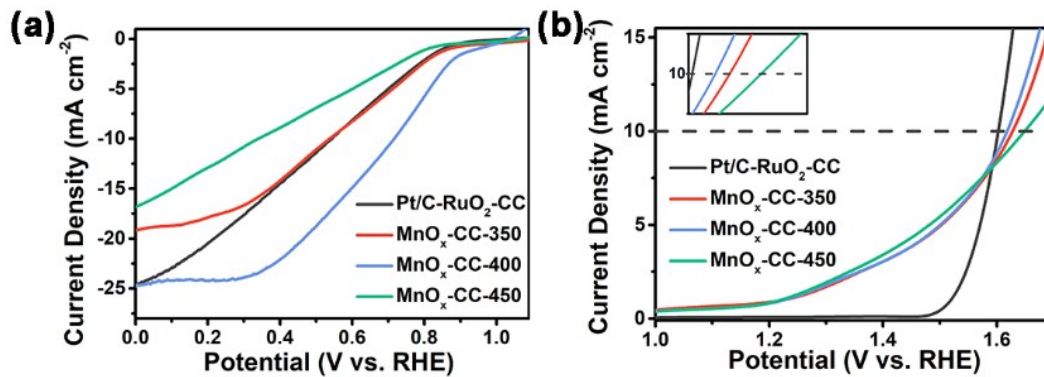


Figure S4. (a) Oxygen reduction reaction and (b) oxygen evolution reaction polarization curves of Pt/C-RuO₂-CC, MnO_x-CC-350 MnO_x-CC-400 and MnO_x-CC-450.

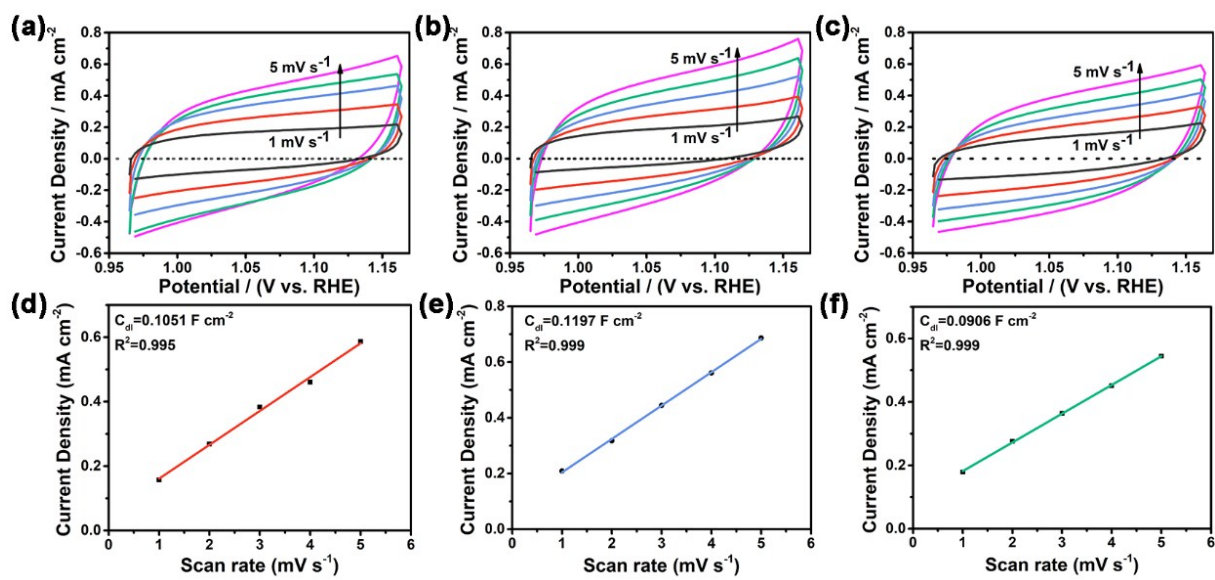


Figure S5. CV curves and double-layer capacitances of (a), (d) MnO_x-CC-350, (b), (e) MnO_x-CC-400 and (c), (f) MnO_x-CC-450.

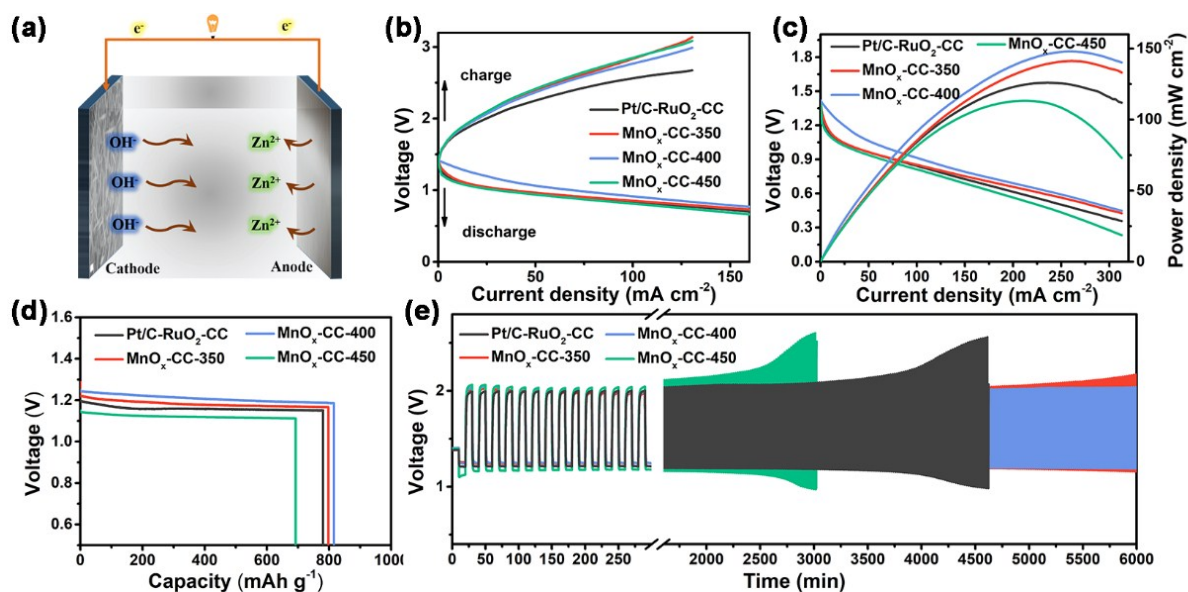


Figure S6. (a) Schematic illustration of the Zn-air battery. (b) Charge and discharge polarization curves, (c) power density, (d) specific capacity at 10 mA cm^{-2} and (e) cycling stability at 5 mA cm^{-2} of Zn-air batteries with various electrocatalysts.

To investigate the practical applications of $\text{MnO}_x\text{-CC}$, a liquid Zn-air battery was assembled with $\text{MnO}_x\text{-CC}$ as air electrode electrocatalyst, a piece of Zn plate as negative electrode with 6 M KOH and 0.2 M $\text{Zn}(\text{CH}_3\text{COO})_2$ electrolyte (Figure S6a). Figure S6b shows the charge and discharge polarization curves of different batteries. The $\text{MnO}_x\text{-CC-400}$ exhibited the smallest discharge–charge voltage gaps among the $\text{MnO}_x\text{-CC}$ samples. The power density of 148 mW cm^{-2} is achieved with the $\text{MnO}_x\text{-CC-400}$ cathode, which is larger than those of Pt/C-RuO₂-CC (126 mW cm^{-2}), $\text{MnO}_x\text{-CC-350}$ (141 mW cm^{-2}) and $\text{MnO}_x\text{-CC-450}$ (113 mW cm^{-2}) (Figure S6c). The specific capacity of Zn-air battery was investigated at a current density of 10 mA cm^{-2} . The Zn-air battery with $\text{MnO}_x\text{-CC-400}$ cathode exhibits the high specific capacity of $816 \text{ mAh g}^{-1}_{\text{Zn}}$ based on the consumed Zn, which is close to the theory value of $825 \text{ mAh g}^{-1}_{\text{Zn}}$. The specific capacities of other batteries with Pt/C-RuO₂-CC, $\text{MnO}_x\text{-CC-350}$ and $\text{MnO}_x\text{-CC-450}$ are 781, 798 and 693 mAh

$\text{g}^{-1}_{\text{Zn}}$, respectively. Figure S5d displays the long-term stability test at the current density of 5 mA cm^{-2} . The Zn-air battery with $\text{MnO}_x\text{-CC-400}$ air cathode demonstrated the good cycling stability with the initial discharge potential of 1.25 V and charge potential of 2.0 V , and no obvious voltage decay is observed after 100 cycles. In contrast, the voltage gaps of Zn-air batteries with Pt/C- $\text{RuO}_2\text{-CC}$ and $\text{MnO}_x\text{-CC-450}$ cathode increase sharply after 70 and 48 h, respectively, suggesting the poor cycling stability.

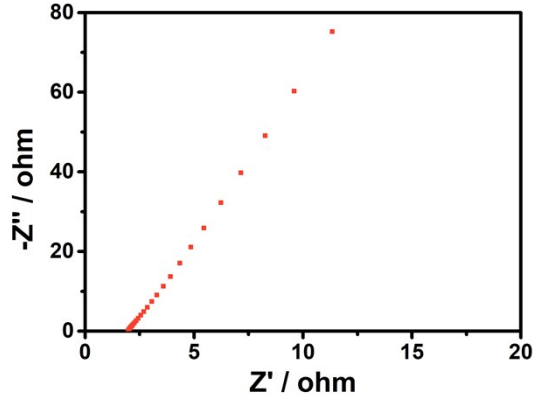


Figure S7. Nyquist plot of polymer electrolyte in the frequency range from 100 kHz to 0.1 Hz with steel/polymer electrolyte/steel system.

The ionic conductivity of polymer electrolyte can be determined by the solution resistance (R_s) from the impedance spectra. The calculation equation is expressed as

$$\sigma = \frac{l}{RA}$$

where σ is conductivity, l is thickness of the solid-state zinc-air battery, R is the solution resistance equal to the intercept on the horizontal axis in Nyquist plot and A is the work area of the battery.

Thus, the conductivity of our polymer electrolyte is around 0.1 S cm^{-1} .

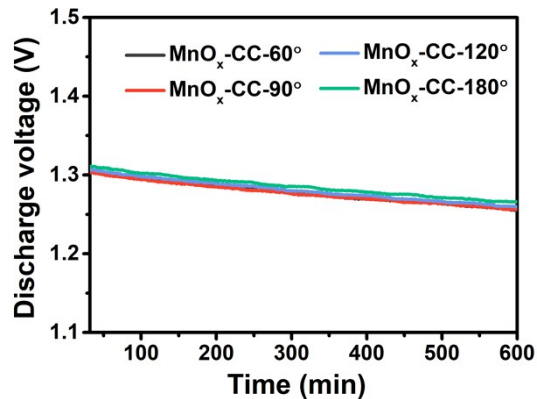


Figure S8. The discharge curves of zinc-air battery at a current density of 1 mA cm^{-2} under different bending angles.

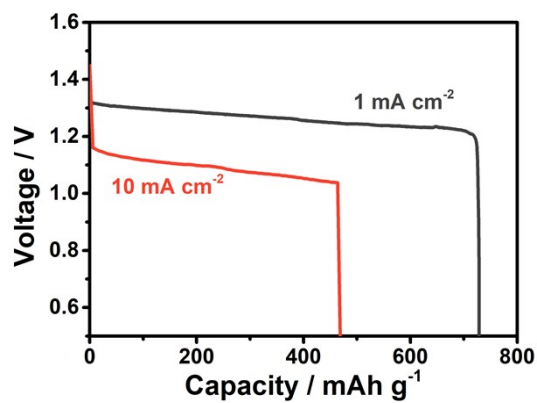


Figure S9. The specific capacities of $\text{MnO}_x\text{-CC-400}$ under different current densities.

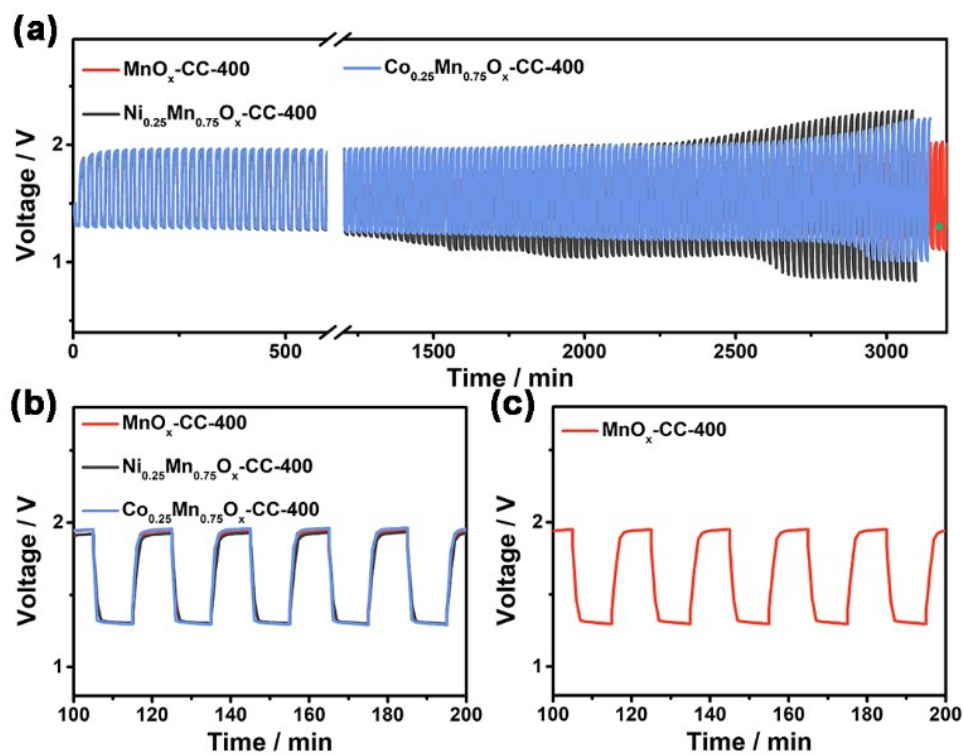


Figure S10. (a) Charge-discharge curves, (b) and (c) the enlarged curves of solid-state zinc-air batteries by using manganese oxide electrocatalysts with or without doping.

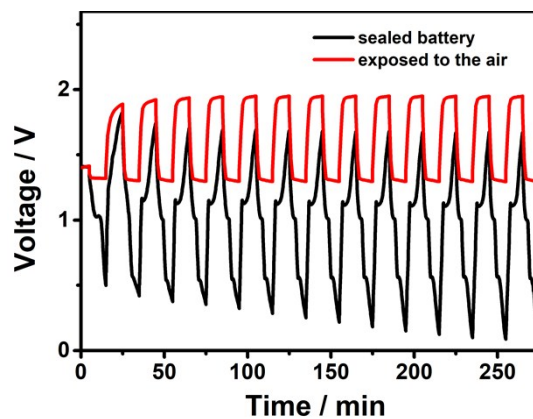


Figure S11. The charge-discharge curves of solid-state batteries with and without oxygen.

The working voltage is distorted obviously when sealed the cathode to prevent the air getting in.

The results demonstrate that the battery is based on the oxygen reduction and evolution reactions.

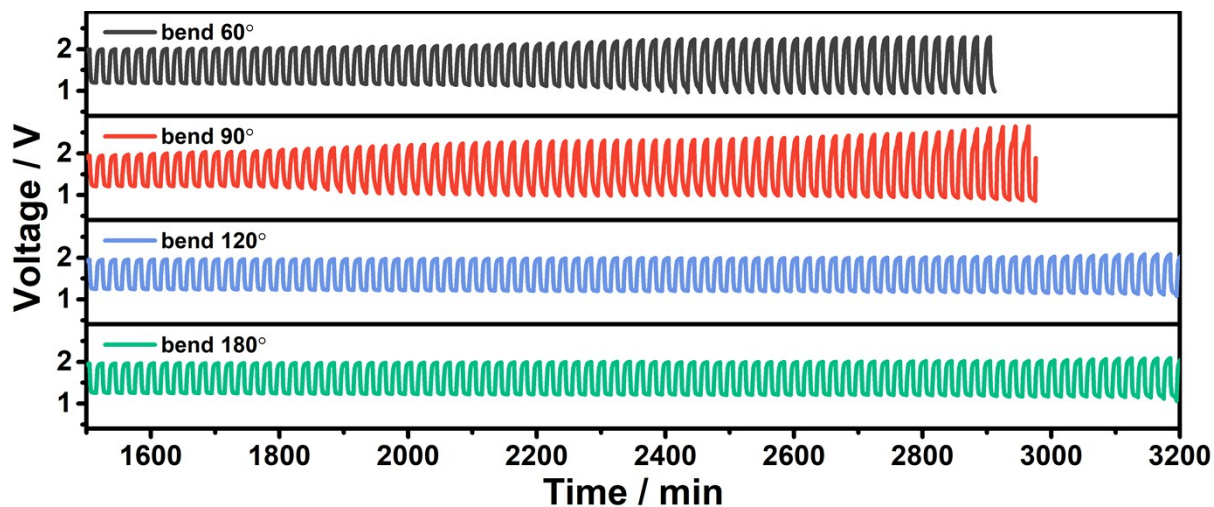


Figure S12. Stability tests of flexible zinc-air batteries under different bending angles (the enlarged section in Figure 7c).

Table S1. Values for R_s , R_{ct} and C_{dl}^* obtained by fitting the EIS data of zinc-air battery.

Cathode	R_s (Ω)	R_{ct} (Ω)	C_{dl}^* (μF)
Pt/C-RuO ₂ -CC	5.286	85.04	171.1
MnO _x -CC-0°	5.357	27.11	202.1
MnO _x -CC-60°	5.354	25.11	220.8
MnO _x -CC-90°	5.516	23.35	208.1
MnO _x -CC-120°	5.351	22.74	256.0
MnO _x -CC-180°	5.472	19.80	271.4

Table S2. The electrochemical performances of solid-state zinc-air batteries with different cathodes.

Sample	Open circuit voltage (V)	Discharge voltage (V)	Cycling stability	Ref.
MnO _x grown on carbon cloth	1.47	1.3	20 min per cycle for 135 cycles (1 mA cm ⁻²)	This work
MnO _x grown on graphene-coated carbon cloth	1.427	1.3	20 min per cycle for 175 cycles (0.7 mA cm ⁻²)	1
Hollow Co ₃ O ₄ nanosphere embedded in carbon arrays	1.44	~	20 min per cycle for 60 cycles (1 mA cm ⁻²)	2
Electrospun CaMnO ₃ Nanotubes	1.32	~	10 h (1 mA cm ⁻²)	3
NiCo ₂ O ₄ nanowires and NiMn LDH nanosheets	1.2	~	10 min per cycle for 30 cycles (0.5 mA cm ⁻²)	4
porphyrin covalent organic framework	1.39	1.22	~	5
Mesoporous Co ₃ O ₄ layers coupled with N-rGO nanosheets	1.33	1.2	20 min per cycle for 75 cycles (3 mA cm ⁻²)	6
Co ₃ O ₄ -embedded N-doped porous carbon grown on carbon cloth	1.41	1.11	10 min per cycle for 60 cycles (20 mA cm ⁻²)	7

References

1. A. Sumboja, M. Lübke, Y. Wang, T. An, Y. Zong and Z. Liu, *Adv. Energy Mater.*, 2017, **7**, 1700927.
2. C. Guan, A. Sumboja, H. Wu, W. Ren, X. Liu, H. Zhang, Z. Liu, C. Cheng, S. J. Pennycook and J. Wang, *Adv. Mater.*, 2017, **29**, 1704117.
3. S. Peng, X. Han, L. Li, S. Chou, D. Ji, H. Huang, Y. Du, J. Liu and S. Ramakrishna, *Adv. Energy Mater.*, 2018, **8**, 1800612.
4. X. Guo, T. Zheng, G. Ji, N. Hu, C. Xu and Y. Zhang, *J. Mater. Chem. A*, 2018, **6**, 10243-10252.
5. B.-Q. Li, S.-Y. Zhang, B. Wang, Z.-J. Xia, C. Tang and Q. Zhang, *Energy Environ. Sci*, 2018, **11**, 1723-1729.
6. Y. Li, C. Zhong, J. Liu, X. Zeng, S. Qu, X. Han, Y. Deng, W. Hu and J. Lu, *Adv. Mater.*, 2018, **30**.
7. L. Zhu, D. Zheng, Z. Wang, X. Zheng, P. Fang, J. Zhu, M. Yu, Y. Tong and X. Lu, *Adv. Mater.*, 2018, **30**, e1805268.